Journal of

Applied and Computational Mechanics

Research Paper

Slip Effect on EMHD Tri-Hybrid Non-Newtonian Nanofluid Flow over a Porous Stretching-Slendering Sheet

Galal M. Moatimid⊙, Hamed M. Sayed⊙

Department of Mathematics, Faculty of Education, Ain Shams University, Roxy, Cairo, Egypt
Email: gal_moa@edu.asu.edu.eg (G.M.M.); hamedali@edu.asu.edu.eg (H.M.S.)

Abstract. The motivation of the current work is the flow over a slender surface, which includes the manufacture of optical fibers, polymer sheets, photoelectric devices, wire coatings, solar cells, and fiber sheets. In order to enhance the results of the wire coating process, it is necessary to carefully examine the mass and thermal heat transmission rates. The novelty of this study is the ability to forecast complex thermal issues in the tri-hybrid Sutterby nanofluid flow, considering the effects of electro-hydromagnetic and multi-slip circumstances. The study examines the impact of nonlinear thermal radiation, electric field, and slips in velocity, temperature, and solutal properties on the steady flow confined to two-dimensions Au-TiO$_2$-GO/SA in the field of electro-magneto-hydrodynamics. Employing similarity transformations, the regulatory boundary layer equations are converted to nonlinear ODEs. Following that, the resulting equations are solved using the homotopy perturbation method. Numerical simulations are performed for several physical parameter values, and the influences of numerous distributions are examined. It is observed that the thermal distribution exhibits a decreasing trend as the values of the mixed convection flow, electric field, temperature jump, and velocity slip parameters are boosted. Moreover, the Sherwood number is declining by m, De, δ_1, δ_2, δ_3 and rising due to the enhancement of E_1, γ_1 and γ_3.

Keywords: Sutterby fluid; Tri-hybrid nanoparticles; Electromagnetohydrodynamics; Slandering stretching sheet; Slip conditions.

1. Introduction

Several nonlinear liquid models were put out to depict the viscoelastic properties of complex liquids. The Sutterby nanofluid (SN), one of the non-Newtonian fluid (NNF) models, was utilized to examine the fundamental characteristics of dilatant liquids. The SN's flow was thoroughly investigated by numerous researchers. Two coaxially rotating stretching disks were used to the flow of the SN with an employed magnetic field was investigated [1]. The thermal features of the movement of Williamson SN across the Darcy-Forchheimer sponge intermediate over an extended surface, theoretical together computational analysis, were scrutinized [2]. Considerations were made for the convective boundary, radiation heat flow, and Cattaneo-Christov (CC) heat flux. The originality of this work was shown by combining Williamson SN with a mild homogenous diffusion of nanoparticles and microorganisms. The SN flow and heat transmission problem on a porous moving sheet when magnetohydrodynamics (MHD) and thermal radiation were presented [3]. The Stefan blowing phenomenon occurs when electrically conducting SN material flows over a stretchy rotating disk was showed [4]. The Buongiorno model in determining the role of nanoparticles was examined [5]. A numerical technique was used to convey the solution of the velocity, temperature, and singular fields. It analyzed how the stretched cylinder affected the SN thermal properties. A slip bio convective movement of a NNF layer containing motile microorganisms. The flowing layer traverses stretch of a curved surface was conducted [6]. The study of an incompressible SN's bio convection flow on a surface that may be stretched was investigated [7]. The study also considered the presence of both nanomaterial and bacteria. The fluid permeated a porous area and experienced a consistent vertical magnetic field's influences. The SN bioconvective flow includes some unique biotechnological and bioengineering applications was explored [8]. Analysis of the flow across a stretched cylinder of the SN boundary layer via the updated Heat and mass transfer (HMT) models and the CC theory was scrutinized [9]. The physical phenomenon was initially generated in the procedure of partial differential equations (PDEs) by utilizing the conservation laws, and a calculated prototype was created beneath the boundary layer examination. Utilizing magnetic nanofluid flow, nanotechnology's adaptability, and magnetic fields' manipulation capabilities are combined to tackle obstacles and generate inventive solutions in diverse manufacturing. The study suggested scrutinizing a hybrid nanofluid's flow with magneto-micropolar properties over a surface that is elongating [10]. A squeezing channel, also known as a flow route with variable width, exhibits distinct fluid behavior that introduces novel opportunities and challenges for optimization when compared to conventional channels [11]. The HMT of SN caused by a stretched horizontal surface together with microorganisms bioconvection was discovered

[12]. The study focused on examining how the form of nanoparticles affects the movement of a micropolar hybrid nanofluid past a vertical plate [13]. According to the SN, an incompressible micropolar nano NNF transported peristaltically was studied by Dabe et al. [14].

A mathematical model was sophisticated to assess the importance of tri-hybrid nanoparticles (THN) in thermal control [15]. The Tiwari and Das model was selected for nanoparticle modelling. The THN exhibited exceptional thermal conductivity. The study investigated the concurrent transmission of the MHD in nanolayers caused by factors such as shape, motile microorganisms, and MHD [16]. The discussion focused on the significant impact of viscous dissipation caused by effects of Joule heating on THN flow, taking into account the model's and the nanolayer's respective thermal conductivities. The applications of THN were extensive and include heat exchangers, slurries, vehicle radiators, cooling systems, electronic chips, and biomedicine. The study investigated the movement of MHD-hybrid nanomaterial over a surface that was heated through convection, using an entropy formulation [17]. The Dufour and Soret effects were taken into consideration as study investigated the behavior of a pseudo-plastic fluid flowing on a stretched porous surface [18]. THN has superior thermal properties, higher stability, increased physical robustness, and multifunction nullity in comparison to hybrid or conventional nanofluids. The study investigated the thermal properties of hybrid nanofluid and THN as they pass through a porous material [19]. While nanofluid performance has been widely acknowledged and demonstrated positive outcomes in heat transport phenomena, researchers were exploring the use of organized nanoparticles suspension in a base fluid to boost the thermal performance of traditional fluids [20]. The optimization of shear rate scrutiny was performed for carbon nanotube micropolar nanofluids based on water using an extending surface [21]. The utilization of these nanofluids in nanofluids has introduced distinctive heat and mechanical characteristics that have attracted considerable interest in diverse engineering implementations. The contemporary period of scientific advancements relies heavily on the effective rate of heat transfer in miscellaneous engineering applications, where nanofluids play a significant role. An investigation was carried out using an artificial neural network to determine the effect of particle concentration on the optimization of transmission of heat analysis in a water-based hybrid nanofluid [22]. Nanofluids were considered to be a superior energy-transfer medium for the future, mainly because of their outstanding thermodynamic characteristics. The investigating of heat transmission on elongated surfaces was significant owing to its use in several sectors such as industry, manufacturing, and medicine [23]. The investigation was conducted to analyze the influences of magnetic and electrical fields, heat radiation, viscous dissipation, and Joule heating on the flow upon a nonlinear stretched surface with varying thicknesses. The analysis was performed using Cu/water as a nanofluid.

The investigation examined the flow between vertical parallel plates of a hybrid nanofluid including magnesium oxide and gold nanoparticles [24]. The work's applications encompassed innovative heat duct technologies for processing in the fields of nuclear, biomedical, and engineering processes. Sodium alginate third-grade NNF was selected as base fluid. The impact of electro-magneto hydrodynamics was considered. The spatial distribution of particles in a fluid was predominantly non-uniform. The rough distribution of solid particles has an influence on both the velocity distribution and the heat transmission of the fluid. The study emphasized the impact of altering the particles density interior a liquid [25]. The fluid traversed a sinuous curved conduit with the existence of an externally imposed magnetic field. The topic of heat transport was explored in relation to varying thermal conductivity. The study investigated the interactions between flow, magnetic, and electric fields, as well as the practical uses of the ensuing phenomenon in microfluidics [26]. When an electric current passes through an electrolyte with a magnetic field, it creates a Lorentz body force which can cause fluid electrohydrodynamic motion and pressure variations. The study also conducted a brief evaluation of the influence of magnetic resonance imaging on blood circulation. Electrolytes MHD was an extremely multidisciplinary field that integrates concepts from electro kinetics, electrochemistry, fluid mechanics, and equations of Maxwell. The introduction of a new formularization of vortical fluid and relativistic spinful to relativistic MHD was extended in a recent study [27]. It was documented that the electro-Magneto-Hydrodynamics (EMHD) micropump operated parallel to the flow of an electrically conducting liquid when perpendicular magnetic and electric fields were applied [28]. These studies described a brand-new micropump with an MHD-based pumping mechanism.

In the application of foundational physical laws and the computational equations of an extensive variety of problems in biomedical manufacturing, applied mathematics, and mathematical physics, PDEs were frequently occurring. This topic was essential to analysis, modern mathematical disciplines, geometry, and physics. PDEs could be used to model a wide range of physical circumstances with the appropriate starting and/or boundary conditions. A big and crucial difficulty in nonlinear optics was the development of an inventive mathematical method to determine the exact or approximate solutions of nonlinear PDEs. Unfortunately, there were no clear solutions to these problems. It was also necessary to use other strategies, including numerical and perturbation methodologies. The HPM was suggested by He [29-31] as a solution to the problems with the conventional perturbation approach. There were many benefits of HPM over other conventional analytical techniques. It was a series expansion technique independent of the size of the physical factors. Therefore, it could be used to handle both weakly and substantially nonlinear circumstances. The choice of the chosen basic functions for the solutions and the appropriate auxiliary linear operator of homotopy was made possible with a considerable amount of flexibility. Remarkably fluid expression and explicit acquisition of the answer were allowed. In addition to being consistent with other approaches for solving nonlinear PDEs/ordinary differential equations (ODEs), such as Padé approximants and spectral approaches, the HPM offered a straightforward mechanism to guarantee the convergence of obtained solution. It has been demonstrated that it was used to address a diversity of engineering issues, containing highly nonlinear vibration and noise problems. The study examined the flow of Walters' B NNF, which is incompressible, in a rotating annulus [32]. The fluid flows through porous media and is subjected to a regular magnetic field perpendicular to its direction. The inclusion of mass transmission was incorporated into the compositions of both heterogeneous and homogeneous chemical reactions, taking into account the thermal diffusion effect. An analysis was conducted on the microorganisms' motion, as well as the nano NNF' MHD free convective peristaltic motion that follows the Carreau prototype [33]. The study's innovation stems from examining the interaction of microorganisms, such as viruses, bacteria, and microbes, with velocity, thermal, and nanoparticle distributions. This analysis aims to differentiate the positive or negative effects that microorganisms and nanoparticles have on the flow via peristaltic pipes. The study presented the movement of a boundary layer in an incompressible nano Williamson NNF [34]. The boundary layer formed on a vertical surface that was extending exponentially and porous. Motile microorganisms were shown to be responsible for the movement within a permeable medium, as indicated by the modified Darcy law. A study demonstrated the motion of an incompressible Prandtl-Eyring NNF across a porous plate that is either expanding or decreasing [35]. The flow was subjected to supplementary couple stress, modified by a homogeneous regular magnetic field, and permeated by a permeable material. The strategy described in several publications within the HPM is able to address the issue of computational complexity, since it necessitates less computer memory and achieves faster calculation times compared to earlier methods. Therefore, it is straightforward, potent, efficient, and encouraging. Therefore, the utilization of the HPM offers numerous benefits.

The investigation of HMT has received incredible attention among physicists, engineers, and mathematicians due to its wide range of implications. These technologies have been extensively used in a variety of industrial processes. Many researchers have

published significantly on these occurrences while considering various materials. The innovative attribute of the current study is therefore the prediction of the advanced thermal properties of the ternary-hybrid Sutterby fluid flow under the influence of electro-hydromagnetic and multi-slip conditions. On the steady two-dimensional EMHD flow of Au-TiO₂-GO/SA tri-Hybrid Sutterby nanofluid (THSN), integrated influences of nonlinear thermal radiation, electric field, and velocity, thermal, and solutal second slip-order boundary conditions are taken into consideration. The THSN is affected by this mixture when applied to a porous, thin, stretchy sheet. The study is structured on the following research questions:

- What impact does an applied electric field have on the thermal and hydrodynamic properties of Au-TiO₂-GO/SA THSN?
- How do the second slip conditions behave with respect to the velocity, thermal, and solutal of Au-TiO₂-GO/SA THSN?
- How the flow profiles and regular physical quantities of Au-TiO₂-GO/SA THSN are impacted by the significant parameters?

The remaining sections of this article are arranged as follows: Using the most important motion equations and significant physical factors, § 2 illustrates the mathematical procedure and the suitable similarity modifications that update the perception of PDEs relative to conventional ones. The closed form solutions to the aforementioned system of equations and specified boundary conditions are shown in § 3 with regard to HPM. § 4 reviews and explains the findings while offering some physical perspectives on the issue. § 5 is where the key summaries and conclusions are presented.

2. Mathematical Formulation

Consider about the incompressible ternary-hybrid Sutterby nanofluid flowing through a stretching, slandering sheet with varying thickness, $y = \delta(x + d)^{(1-n)/2}$, in a non-linear steady two-dimensional laminar EMHD flow, embedded in Darcy porous medium with multiple slips. The plate is being elongated with velocity $u_w(x) = U_0(x + d)^n$, where δ very small number. likewise, it is presumable that the model can only be valid with $n \neq 1$, as $n = 1$ it becomes straightforward to the flat sheet case. The following nanofluids have been considered: gold (Au), titanium dioxide (TiO₂), graphite oxide (GO), and sodium alginate (SA). Sutterby fluid is an opposite model for the base fluid (SA), which is a shear thinning and thickening fluid. Moreover, it is presupposed that there is no slip between the nanoparticles and the base fluid, which are in local equilibrium of thermal. $B(x)$ is operated normally to the slender surface. A small magnetic Reynolds number indicates that the induced magnetic field will be negligible compared to the applied magnetic field. The slender sheet surface is subjected to a consistent concentration of nanoparticle and temperature. Both the ambient concentration and temperature are lower than these values. As shown in Fig. 1, it is assumed that the x-axis represents the direction of the sheet motion, and the y-axis is perpendicular to it.
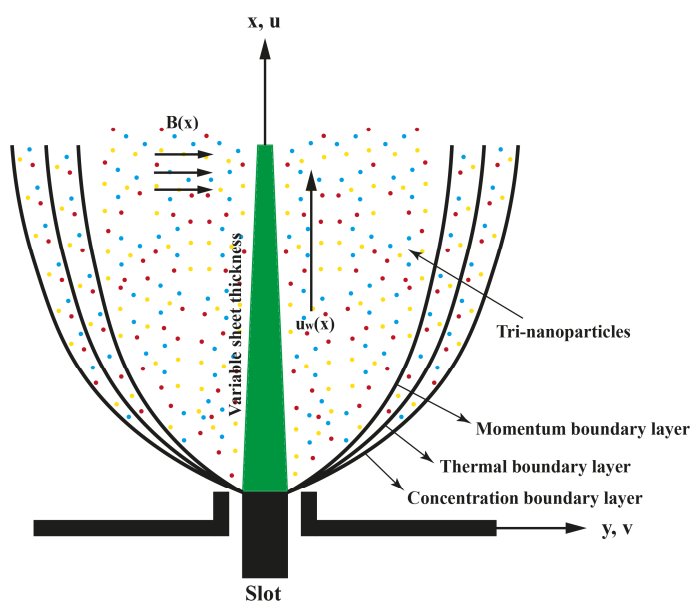
The governing nonlinear differential equations for THSN flow are depicted as:

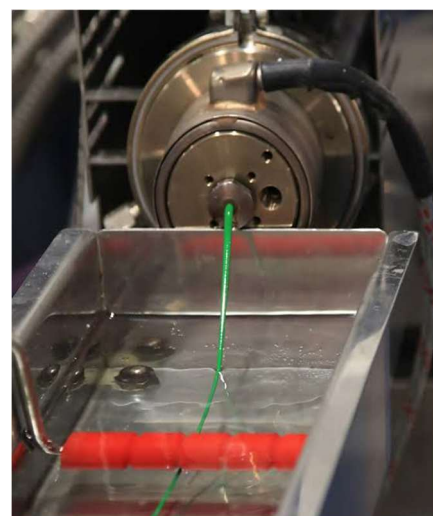$$\frac{\partial u}{\partial x} + \frac{\partial v}{\partial y} = 0, \tag{1}$$

$$u\frac{\partial u}{\partial x} + v\frac{\partial u}{\partial y} = \frac{\mu_{tnf}}{\rho_{tnf}} \frac{1}{2} \frac{\partial^2 u}{\partial y^2}\left(1 - \frac{m b^2}{2}\left(\frac{\partial u}{\partial y}\right)^2\right) + \frac{B\sigma_{tnf}}{\rho_{tnf}}(E - Bu) - \frac{\mu_{tnf}}{K\rho_{tnf}}u + g\left((\beta_T)_{tnf}(T - T_\infty) + (\beta_C)_{tnf}(C - C_\infty)\right), \tag{2}$$

$$u\frac{\partial T}{\partial x} + v\frac{\partial T}{\partial y} = \frac{1}{(\rho C_p)_{tnf}}\left(k_{tnf} + \frac{16\sigma_e T_\infty^3}{3\beta_R}\right)\frac{\partial^2 T}{\partial y^2} + \frac{\sigma_{tnf}}{(\rho C_p)_{tnf}}(E - Bu)^2 + \tau\left(D_B \frac{\partial C}{\partial y}\frac{\partial T}{\partial y} + \frac{D_T}{T_\infty}\left(\frac{\partial T}{\partial y}\right)^2\right), \tag{3}$$

$$u\frac{\partial C}{\partial x} + v\frac{\partial C}{\partial y} = D_B \frac{\partial^2 C}{\partial y^2} + \frac{D_T}{T_\infty}\frac{\partial^2 T}{\partial y^2}. \tag{4}$$

(a)   (b)

Fig. 1. (a) THSN flow through slandering stretching cylinder, (b) Extrusion cooling process.

Table 1. Density, thermal expansion coefficient, thermal conductivity, specific heat capacity, and electrical conductivity of sodium alginate, gold, titanium dioxide, and graphite oxide nanoparticles [36-38].

Physical properties	SA	Au	TiO$_2$	GO
Density	989	19300	4250	1800
Thermal expansion coefficient	99×10^{-5}	1.4×10^{-5}	0.9×10^{-5}	28.4×10^{-5}
Thermal conductivity	0.6376	318	8.9538	5000
Specific heat capacity	4175	129.1	686.2	717
Electrical conductivity	2.6×10^{-4}	4.52×10^{7}	2.6×10^{6}	1.1×10^{-5}
Prandtl number	6.135			

The corresponding boundary conditions are:

$$u = u_w(x) + k_1\left(\frac{\partial u}{\partial y}\right) - J_1\left(\frac{\partial^2 u}{\partial y^2}\right), \ T = T_w(x) + k_2\left(\frac{\partial T}{\partial y}\right) - J_2\left(\frac{\partial^2 T}{\partial y^2}\right),$$

$$C = C_w(x) + k_3\left(\frac{\partial C}{\partial y}\right) - J_3\left(\frac{\partial^2 C}{\partial y^2}\right), \ v = 0 \ \text{at} \ y = \delta(x+d)^{(1-n)/2}, \tag{5}$$

$$u = 0, T = T_w, C = C_w \ \text{at} \ y \to \infty,$$

where,

$$k_i = \left(\frac{2-\beta_i}{\beta_i}\right)\eta_i(x+d)^{\frac{1-n}{2}}, \ J_i = \frac{1}{2}\eta_i(x+d)^{1-n}, \ \eta_{i+1} = \frac{2\lambda}{\lambda+1}\frac{\eta_i}{pr}; i = 1,2,3,$$

$$B(x) = B_0(x+d)^{\frac{n-1}{2}}, \ E(x) = E_0(x+d)^{\frac{n-1}{2}}, \ K(x) = k_0(x+d)^{1-n}, \tag{6}$$

$$T_w(x) = T_\infty + T_0(x+d)^{\frac{1-n}{2}}, \ C_w(x) = C_\infty + C_0(x+d)^{\frac{1-n}{2}}.$$

The tri-nanofluid is thought to be a well combined, diluted colloidal combination of Au-TiO$_2$-GO nanogranules in a base fluid called SA. The specific number for the thermophysical characteristics of the base fluid SA and the nanoparticles of Au-TiO$_2$-GO might be identified in Table 1.

Following are correlations that explain the thermophysical characteristics of trihybrid nanofluids [39]:

$$\rho_{tnf} = (1-\varphi_3)\left[(1-\varphi_2)\left((1-\varphi_1)\rho_f + \varphi_1\rho_1\right) + \varphi_2\rho_2\right] + \varphi_3\rho_3,$$

$$\mu_{tnf} = \mu_f\left[(1-\varphi_1)(1-\varphi_2)(1-\varphi_3)\right]^{-2.5},$$

$$(\rho\beta)_{tnf} = (1-\varphi_3)\left[(1-\varphi_2)\left((1-\varphi_1)(\rho\beta)_f + \varphi_1(\rho\beta)_1\right) + \varphi_2(\rho\beta)_2\right] + \varphi_3(\rho\beta)_3,$$

$$(\rho C_p)_{tnf} = (1-\varphi_3)\left[(1-\varphi_2)\left((1-\varphi_1)(\rho C_p)_f + \varphi_1(\rho C_p)_1\right) + \varphi_2(\rho C_p)_2\right] + \varphi_3(\rho C_p)_3,$$

$$\sigma_{tnf} = \sigma_{hnf}\left[\frac{\sigma_3 + 2\sigma_{hnf} - 2\varphi_3(\sigma_{hnf} - \sigma_3)}{\sigma_3 + 2\sigma_{hnf} + \varphi_3(\sigma_{hnf} - \sigma_3)}\right], \ \sigma_{hnf} = \sigma_{nf}\left[\frac{\sigma_2 + 2\sigma_{nf} - 2\varphi_2(\sigma_{nf} - \sigma_2)}{\sigma_2 + 2\sigma_{nf} + \varphi_2(\sigma_{nf} - \sigma_2)}\right],,$$

$$\sigma_{nf} = \sigma_f\left[\frac{\sigma_1 + 2\sigma_f - 2\varphi_1(\sigma_f - \sigma_1)}{\sigma_1 + 2\sigma_f + \varphi_1(\sigma_f - \sigma_1)}\right],$$

$$k_{tnf} = k_{hnf}\left[\frac{k_3 + 2k_{hnf} - 2\varphi_3(k_{hnf} - k_3)}{k_3 + 2k_{hnf} + \varphi_3(k_{hnf} - k_3)}\right], \ k_{hnf} = k_{nf}\left[\frac{k_2 + 2k_{nf} - 2\varphi_2(k_{nf} - k_2)}{k_2 + k_{nf} + \varphi_2(k_{nf} - k_2)}\right],$$

$$k_{nf} = k_f\left[\frac{k_1 + 2k_f - 2\varphi_1(k_f - k_1)}{k_1 + k_f + \varphi_1(k_f - k_1)}\right],$$

where indicating the characteristics of solid gold, titanium dioxide, and graphite oxide nanoparticles, respectively, are the numerical subscripts 1, 2, and 3. The following similarity transformations are introduced in order to turn the Eqs. (1) to (5) into a collection of nonlinear ODEs [40-45]:

$$\eta = y\left(\frac{n+1}{2}\frac{U_0}{\nu_f}(x+b)^{n-1}\right)^{\frac{1}{2}}, \ \psi(\eta) = f(\eta)\left(\frac{2}{n+1}U_0\nu_f(x+b)^{n+1}\right)^{\frac{1}{2}}, \ \theta = \frac{T-T_\infty}{T_w(x)-T_\infty}, \ \phi = \frac{C-C_\infty}{C_w(x)-C_\infty}. \tag{7}$$

The stream function ψ is expressed as $u = \partial\psi/\partial y$ and $v = -\partial\psi/\partial x$, which satisfies the equation of continuity. The resulting u and v are:

$$u = U_0(x+d)^n f'(\eta), \ v = -\left(\frac{n+1}{2}U_0\nu_f(x+b)^{n-1}\right)^{1/2}\left(f(\eta) + \frac{n-1}{n+1}\eta f'(\eta)\right), \tag{8}$$

With the help of Eqs. (7) and (8), Eqs. (1) to (4) in association with the boundary conditions (5) readily take the forms:

$$\frac{\mu_{tnf}}{\mu_f}\frac{\rho_f}{\rho_{tnf}}\frac{1}{2}\left(1-\frac{n+1}{4}mDef''^2\right)f''' -\frac{2n}{n+1}f'^2 + ff'' -\left(\frac{\sigma_{tnf}}{\sigma_f}\frac{\rho_f}{\rho_{tnf}}M+\frac{\mu_{tnf}}{\mu_f}\frac{\rho_f}{\rho_{tnf}}k_1^*\right)f'+\frac{\sigma_{tnf}}{\sigma_f}\frac{\rho_f}{\rho_{tnf}}ME_1 + \frac{\rho_f}{\rho_{tnf}}\frac{(\rho\beta)_{tnf}}{(\rho\beta)_f}\frac{2\chi}{n+1}(\theta+N\phi)=0, \tag{9}$$

$$\frac{(\rho C_p)_f}{(\rho C_p)_{tnf}}\frac{1}{Pr}\left(\frac{k_{tnf}}{k_f}+Rd\right)\theta'' + \frac{n-1}{n+1}f'\theta + f\theta' + \frac{\sigma_{tnf}}{\sigma_f}\frac{(\rho C_p)_f}{(\rho C_p)_{tnf}}MEc\left(f'-E_1\right)^2 + Nb\phi'\theta' + Nt\theta'^2 = 0, \tag{10}$$

$$\frac{1}{Sc}\left(\phi''+\frac{Nt}{Nb}\theta''\right)+\frac{n-1}{n+1}f'\phi + f\phi' = 0. \tag{11}$$

The following are the amended boundary conditions:

$$f'(\Gamma)=1+\delta_1 f''(\Gamma)+\gamma_1 f'''(\Gamma),\quad f(\Gamma)=\Gamma\left(\frac{1-n}{1+n}\right)\left(1+\delta_1 f''(\Gamma)+\gamma_1 f'''(\Gamma)\right),$$

$$\theta(\Gamma)=1+\delta_2\theta'(\Gamma)+\gamma_2\theta''(\Gamma),\quad \phi(\Gamma)=1+\delta_3\phi'(\Gamma)+\gamma_3\phi''(\Gamma), \tag{12}$$

$$f'(\infty)=0,\quad \theta(\infty)=0,\quad \phi(\infty)=0.$$

where $\delta_i=\left(\frac{2-\alpha_i}{\alpha_i}\right)\eta_i\left(\frac{n+1}{2}\frac{U_0}{\nu_f}\right)^{\frac{1}{2}}$, $\gamma_i=-\frac{1}{2}\eta_i^2\left(\frac{n+1}{2}\frac{U_0}{\nu_f}\right)$; $i=1,2,3$, and $\Gamma=\delta\left(\frac{n+1}{2}\frac{U_0}{\nu_f}\right)^{\frac{1}{2}}$.

In Eqs. (9) to (12), $De, k_1^*, E_1, M, Gr_T, Gr_C, \chi, N, Re_x, Rd, Ec, Pr, Nt, Sc,$ and Nb are expressed below:

$$k_1^*=\frac{2\nu_f}{(n+1)U_0 k_0},\quad M=\frac{2\sigma_f B_0^2}{\rho_f U_0(n+1)},\quad E_1=\frac{E_0}{B_0 U_0(x+d)^n},\quad De=\frac{U_0^3(x+d)^{3n-1}b^2}{\nu_f},\quad Gr_T=\frac{g(\rho\beta_T)_f(T_w-T_\infty)(x+d)^3}{\rho_f\nu_f},$$

$$Gr_C=\frac{g(\rho\beta_C)_f(C_w-C_\infty)(x+d)^3}{\rho_f\nu_f},\quad Re_x=\frac{u_{w(x+d)}}{\nu_f},\quad \chi=\frac{Gr_x}{Re_x^2},\quad N=\frac{Gr_C}{Gr_T},\quad Pr=\frac{(\rho C_p)_f\nu_f}{k_f},\quad Rd=\frac{16\sigma_e T_\infty^3}{3k_f B_R},$$

$$Ec=\frac{u_w^2}{(C_p)_f(T_w-T_\infty)},\quad Nt=\frac{\tau D_T(T_w-T_\infty)}{T_\infty\nu_f},\quad Nb=\frac{\tau D_B C_0}{\nu_f},\quad Sc=\frac{\nu_f}{D_B}.$$

The domain $[\delta,\infty)$ has been transformed to $[0,\infty)$ using $F(\xi)=F(\eta-\Gamma)=f(\eta)$, $\Theta(\xi)=\Theta(\eta-\Gamma)=\theta(\eta)$, $\Phi(\xi)=\Phi(\eta-\Gamma)=\phi(\eta)$ and thus the governing Eqs. (9) to (11) can be rewritten as:

$$\frac{\mu_{tnf}}{\mu_f}\frac{\rho_f}{\rho_{tnf}}\frac{1}{2}\left(1-\frac{n+1}{4}mDeF''^2\right)F''' -\frac{2n}{n+1}F'^2 + FF'' -\left(\frac{\sigma_{tnf}}{\sigma_f}\frac{\rho_f}{\rho_{tnf}}M+\frac{\mu_{tnf}}{\mu_f}\frac{\rho_f}{\rho_{tnf}}k_1^*\right)F'+\frac{\sigma_{tnf}}{\sigma_f}\frac{\rho_f}{\rho_{tnf}}ME_1 + \frac{\rho_f}{\rho_{tnf}}\frac{(\rho\beta)_{tnf}}{(\rho\beta)_f}\frac{2\chi}{n+1}(\theta+N\phi)=0, \tag{13}$$

$$\frac{(\rho C_p)_f}{(\rho C_p)_{tnf}}\frac{1}{Pr}\left(\frac{k_{tnf}}{k_f}+Rd\right)\Theta'' + \frac{n-1}{n+1}F'\Theta + F\Theta' + \frac{\sigma_{tnf}}{\sigma_f}\frac{(\rho C_p)_f}{(\rho C_p)_{tnf}}MEc\left(F'-E_1\right)^2 + Nb\Phi'\Theta' + Nt\Theta'^2 = 0, \tag{14}$$

$$\frac{1}{Sc}\left(\Phi''+\frac{Nt}{Nb}\Theta''\right)+\frac{n-1}{n+1}F'\Phi + F\Phi' = 0. \tag{15}$$

The boundary conditions that are outlined:

$$F'(0)=1+\delta_1 F''(0)+\gamma_1 F'''(0),\quad F(0)=\Gamma\left(\frac{1-n}{1+n}\right)\left(1+\delta_1 F''(0)+\gamma_1 F'''(0)\right),$$

$$\Theta(0)=1+\delta_2\Theta'(0)+\gamma_2\Theta''(0),\quad \Phi(0)=1+\delta_3\Phi'(0)+\gamma_3\Phi''(0), \tag{16}$$

$$F'(\infty)=0,\quad \Theta(\infty)=0,\quad \Phi(\infty)=0.$$

2.1. Significant physical quantities

The skin friction coefficient, local Nusselt number, and the Sherwood number (C_{fx}, Nu_x, Sh_x) are the physical quantities that are practical attention interest. These quantities are defined along the surface of the sheet:

$$C_{fx}=\frac{\tau_w}{\frac{1}{2}\rho u_w^2},\quad Nu_x=\frac{(x+d)q_w}{k_f(T-T_\infty)},\quad Sh_x=\frac{(x+d)j_w}{D_B(C-C_\infty)}\quad \text{at } y=\delta(x+d)^{\frac{1-n}{2}}, \tag{17}$$

where τ_w for surface shear stress, q_w for surface heat flux, and j_w stands for mass flux. These quantities should be expressed using the appropriate formulas:

$$\tau_w = \frac{\mu_{tnf}}{2}\left(\frac{\partial u}{\partial y} - \frac{mb^2}{6}\left(\frac{\partial u}{\partial y}\right)^3\right), \ q_w = -\left(k_{tnf} + \frac{16\sigma_e T_\infty^3}{3\beta_R}\right)\frac{\partial T}{\partial y}, \ j_w = -D_B\left(\frac{\partial C}{\partial y}\right). \tag{18}$$

The reduced C_{fx}, Nu_x and Sh_x in dimensionless form are estimated using Eqs. (7) and (8) and are indicated as follows:

$$C_{fx}Re_x^{\frac{1}{2}} = \frac{\mu_{tnf}}{\mu_f}\sqrt{\frac{n+1}{2}}\left(1 - \frac{n+1}{12}mDeF''(0)^2\right)F''(0), \tag{19}$$

$$Nu_xRe_x^{-\frac{1}{2}} = -\left(\frac{k_{tnf}}{k_f} + Rd\right)\sqrt{\frac{n+1}{2}}\Theta'(0), \tag{20}$$

$$Sh_xRe_x^{-\frac{1}{2}} = -\sqrt{\frac{n+1}{2}}\Phi'(0). \tag{21}$$

3. Solution Procedure Using HPM

We consider a non-linear differential equation as a starting point for the development of a homotopy perturbation method:

$$D(\nu) - h(r) = 0, \ r \in \Lambda. \tag{22}$$

With regard to the boundary condition:

$$A\left(\nu, \frac{\partial \nu}{\partial n}\right) = 0, \ r \in \partial\Lambda, \tag{23}$$

A known analytical function is represented by $h(r)$, while $\partial\Lambda$ denotes the boundary of domain Λ. The normal drawn outwards from Λ is used for differentiation along it, which is represented by $\partial\nu/\partial n$. A general differential operator is represented by $D(\nu)$, and A is a boundary operator.

The operator D is separated into two parts: linear and nonlinear L and N as:

$$D(\nu) = L(\nu) + N(\nu). \tag{24}$$

The following equation depicts the structure of homotopy perturbation:

$$H(\nu, q) = L(\nu) - L(\nu^0) + qL(\nu^0) + q[N(\nu) - f(r)] = 0, \tag{25a}$$

where,

$$H(r,q): \Lambda \times [0,1] \to R. \tag{25b}$$

in which the boundary conditions are satisfied by an initial approximation of the equation, ν^0, and an embedding parameter $q \in [0,1]$. A power series in q can be used to express the solutions to Eq. (25a):

$$\nu = \sum_{m=0}^{\infty} q^m \nu_m.$$

The most accurate approximation to Eq. (25a) is:

$$\nu = \lim_{q \to 1} \nu = \sum_{m=0}^{\infty} \nu_m.$$

The utilization of the HPM is applied to examine the model equations pertaining to motion, heat, and mass transfer. Consequently, the model's computational solution is presently determined through the utilization of Mathematica software.

By applying the HPM on Eqs. (13), (14) and (15), we get the homotopy form as follows:

$$H(F,q) = L_f(F) - L_f(F^0) + qL_f(F^0) + q\left[-\alpha_3 F''^2 F''' - \frac{2n}{n+1}F'^2 + FF'' + \alpha_4 + \alpha_5\theta + \alpha_6\phi\right] = 0, \tag{26}$$

$$H(\Theta,q) = L_\Theta(\Theta) - L_\Theta(\Theta^0) + qL_\Theta(\Theta^0) + q\left[\frac{n-1}{n+1}F'\Theta + F\Theta' + \alpha_8(F' - E_1)^2 + Nb\Phi'\Theta' + Nt\Theta'^2\right] = 0, \tag{27}$$

$$H(\Phi,q) = L_\Phi(\Phi) - L_\Phi(\Phi^0) + qL_\Phi(\Phi^0) + q\left[\alpha_9\Theta'' + \frac{n-1}{n+1}F'\Phi + F\Phi'\right] = 0. \tag{28}$$

The starting approximations and linear operators are taken to be:

$$L_f = \alpha_1\frac{\partial^3}{\partial\xi^3} - \alpha_2\frac{\partial}{\partial\xi}, \ L_\Theta = \alpha_7\frac{\partial^2}{\partial\xi^2}, \ L_\Phi = \frac{1}{Sc}\frac{\partial^2}{\partial\xi^2} \ \text{and} \ F^0 = \Theta^0 = \Phi^0 = 0.$$

here,

$$\alpha_1 = \frac{\mu_{tnf}}{2\mu_f}\frac{\rho_f}{\rho_{tnf}}, \quad \alpha_2 = \frac{\sigma_{tnf}}{\sigma_f}\frac{\rho_f}{\rho_{tnf}}M + \frac{\mu_{tnf}}{\mu_f}\frac{\rho_f}{\rho_{tnf}}k_1^*, \quad \alpha_3 = \frac{n+1}{4}mDe\alpha_1, \quad \alpha_4 = \frac{\sigma_{tnf}}{\sigma_f}\frac{\rho_f}{\rho_{tnf}}ME_1, \quad \alpha_5 = \frac{\rho_f}{\rho_{tnf}}\frac{(\rho\beta)_{tnf}}{(\rho\beta)_f}\frac{2\chi}{n+1},$$

$$\alpha_6 = N\alpha_5, \quad \alpha_7 = \frac{(\rho C_p)_f}{(\rho C_p)_{tnf}}\frac{1}{Pr}\left(\frac{k_{tnf}}{k_f} + Rd\right), \quad \alpha_8 = \frac{\sigma_{tnf}}{\sigma_f}\frac{(\rho C_p)_f}{(\rho C_p)_{tnf}}MEc, \quad \alpha_8 = \frac{Nt}{ScNb}.$$

The approximation solution for each of F, Θ, and Φ as a sum of the power series of q can be constructed in the following:

$$F = F_0 + qF_1 + q^2F_2 + \ldots = \sum_{m=0}^{\infty} q^m F_m, \tag{29}$$

$$\Theta = \Theta_0 + q\Theta_1 + q^2\Theta_2 + \ldots = \sum_{m=0}^{\infty} q^m \Theta_m, \tag{30}$$

$$\Phi = \Phi_0 + q\Phi_1 + q^2\Phi_2 + \ldots = \sum_{m=0}^{\infty} q^m \Phi_m, \tag{31}$$

Substituting Eqs. (29) to (31) into Eqs. (16), (26) to (28), the coefficient of various powers of q is obtained as:

q^0 :

$$F_0''' - \frac{\alpha_2}{\alpha_1}F_0' = 0, \quad \Theta_0'' = 0, \quad \Phi_0'' = 0. \tag{32}$$

and

$$F_0'(0) = 1 + \delta_1 F_0''(0) + \gamma_1 F_0'''(0), F_0(0) = \Gamma\left(\frac{1-n}{1+n}\right)F_0'(0), F_0'(\infty) = 0,$$

$$\Theta_0(0) = 1 + \delta_2\Theta_0'(0) + \gamma_2\Theta_0''(0), \Theta_0(\infty) = 0, \tag{33}$$

$$\Phi_0(0) = 1 + \delta_3\Phi_0'(0) + \gamma_3\Phi_0''(0), \Phi_0(\infty) = 0.$$

q^1 :

$$\alpha_1 F_1''' - \alpha_2 F_1' - \alpha_3 F_0'''F_0''^2 - \frac{2n}{n+1}F_0'^2 + F_0 F_0'' + \alpha_4 + \alpha_5\Theta_0 + \alpha_6\Phi_0 = 0, \tag{34}$$

$$\alpha_7\Theta_1'' + \frac{n-1}{n+1}F_0'\Theta_0 + F_0\Theta_0' + \alpha_8\left(F_0'^2 - 2E_1F_0' + E_1^2\right) + Nb\Phi_0'\Theta_0' + Nt\Theta_0'^2 = 0, \tag{35}$$

$$\frac{1}{Sc}\Phi_1'' + \frac{n-1}{n+1}F_0'\Phi_0 + F_0\Phi_0' + \alpha_9\Theta_0'' = 0, \tag{36}$$

and

$$F_1'(0) = \delta_1 F_1''(0) + \gamma_1 F_1'''(0), F_1(0) = \Gamma\left(\frac{1-n}{1+n}\right)F_1'(0), F_1'(\infty) = 0,$$

$$\Theta_1(0) = \delta_2\Theta_1'(0) + \gamma_2\Theta_1''(0), \Theta_1(\infty) = 0, \tag{37}$$

$$\Phi_1(0) = \delta_3\Phi_1'(0) + \gamma_3\Phi_1''(0), \Phi_1(\infty) = 0,$$

q^2 :

$$\alpha_1 F_2''' - \alpha_2 F_2' - \alpha_3\left(2F_0'''F_0''F_1'' + F_1'''F_0''^2\right) - \frac{4n}{n+1}F_0'F_1' + F_0 F_1'' + F_1 F_0'' + \alpha_5\Theta_1 + \alpha_6\Phi_1 = 0, \tag{38}$$

$$\alpha_7\Theta_2'' + \frac{n-1}{n+1}\left(F_0'\Theta_1 + F_1'\Theta_0\right) + F_0\Theta_1' + F_1\Theta_0' + 2\alpha_8\left(F_0'F_1' - E_1F_1'\right) + Nb(\Phi_0'\Theta_1' + \Phi_1'\Theta_0') + 2Nt\Theta_0'\Theta_1' = 0, \tag{39}$$

$$\frac{1}{Sc}\Phi_2'' + \frac{n-1}{n+1}\left(F_0'\Phi_1 + F_1'\Phi_0\right) + F_1\Phi_0' + F_0\Phi_1' + \alpha_9\Theta_1'' = 0, \tag{40}$$

and

$$F_2{}'(0) = \delta_1 F_2{}''(0) + \gamma_1 F_2{}'''(0), F_2(0) = \Gamma\left(\frac{1-n}{1+n}\right)F_2{}'(0), F_2{}'(\infty) = 0,$$

$$\Theta_2(0) = \delta_2\Theta_2{}'(0) + \gamma_2\Theta_2{}''(0), \Theta_2(\infty) = 0,$$

$$\Phi_2(0) = \delta_3\Phi_2{}'(0) + \gamma_3\Phi_2{}''(0), \Phi_2(\infty) = 0. \tag{41}$$

Solving Eqs. (32), (34), (35), (36), (38), (39) and (40) in their respective boundary conditions yields:

$$F_0 = b_2 e^{b_1\xi} + b_3 e^{-b_1\xi} + b_4, \quad \Theta_0 = b_5 - b_6\xi, \quad \Phi_0 = b_7 - b_8\xi, \tag{42}$$

$$F_1 = e^{b_1\xi}(b_9 + b_{10}\xi) + e^{-b_1\xi}(b_{11} + b_{12}\xi) + b_{13}e^{2b_1\xi} + b_{14}e^{-2b_1\xi} + b_{15}e^{3b_1\xi} + b_{16}e^{-3b_1\xi} + b_{17}\xi^2 + b_{18}\xi + b_{19}, \tag{43}$$

$$\Theta_1 = e^{b_1\xi}(b_{20} + b_{21}\xi) + e^{-b_1\xi}(b_{22} + b_{23}\xi) + b_{24}e^{2b_1\xi} + b_{25}e^{-2b_1\xi} + b_{26}\xi^2 + b_{27}\xi + b_{28}, \tag{44}$$

$$\Phi_1 = e^{b_1\xi}(b_{29} + b_{30}\xi) + e^{-b_1\xi}(b_{31} + b_{32}\xi) + b_{33}\xi^2 + b_{34}\xi + b_{35}, \tag{45}$$

and

$$F_2 = e^{b_1\xi}\left(b_{36} + b_{37}\xi + b_{38}\xi^2\right) + e^{-b_1\xi}\left(b_{39} + b_{40}\xi + b_{41}\xi^2\right) + e^{2b_1\xi}\left(b_{42} + b_{43}\xi\right) + e^{-2b_1\xi}\left(b_{44} + b_{45}\xi\right)$$
$$+ e^{3b_1\xi}\left(b_{46} + b_{47}\xi\right) + e^{-3b_1\xi}\left(b_{48} + b_{49}\xi\right) + b_{50}e^{4b_1\xi} + b_{51}e^{-4b_1\xi} + b_{52}e^{5b_1\xi} + b_{53}e^{-5b_1\xi} + b_{54}\xi^3 + b_{55}\xi^2 + b_{56}\xi + b_{57}, \tag{46}$$

$$\Theta_2 = e^{b_1\xi}\left(b_{58} + b_{59}\xi + b_{60}\xi^2\right) + e^{-b_1\xi}\left(b_{61} + b_{62}\xi + b_{63}\xi^2\right) + e^{2b_1\xi}\left(b_{64} + b_{65}\xi\right) + e^{-2b_1\xi}\left(b_{66} + b_{67}\xi\right)$$
$$+ e^{3b_1\xi}\left(b_{68} + b_{69}\xi\right) + e^{-3b_1\xi}\left(b_{70} + b_{71}\xi\right) + b_{72}e^{4b_1\xi} + b_{73}e^{-4b_1\xi} + b_{74}\xi^4 + b_{75}\xi^3 + b_{76}\xi^2 + b_{77}\xi + b_{78}, \tag{47}$$

$$\Phi_2 = e^{b_1\xi}\left(b_{79} + b_{80}\xi + b_{81}\xi^2\right) + e^{-b_1\xi}(b_{82} + b_{83} + b_{84}\xi^2) + e^{2b_1\xi}\left(b_{85} + b_{86}\xi\right) + e^{-2b_1\xi}\left(b_{87} + b_{88}\xi\right)$$
$$+ e^{3b_1\xi}\left(b_{89} + b_{90}\xi\right) + e^{-3b_1\xi}\left(b_{91} + b_{92}\xi\right) + b_{93}\xi^4 + b_{94}\xi^3 + b_{95}\xi^2 + b_{96}\xi + b_{97}, \tag{48}$$

$q = 1$, is the accurate approximation for the solution:

$$F = F_0 + F_1 + F_2, \Theta = \Theta_0 + \Theta_1 + \Theta_2, \text{and} \ \Phi = \Phi_0 + \Phi_1 + \Phi_2. \tag{49}$$

Due to the length of the mathematical expression for the constants $\{b_i\}_{i=1}^{97}$, it is not mentioned here.

4. Validation of the Outcomes

To verify the accuracy of our work, we contrasted our findings with prior studies as shown in Table 2. The numerical values of $-F''(0)$ and $-\Theta'(0)$ in our findings appear to be more consistent with those of Vajravelu et al. [41].

5. Results and Discussions

The velocity, temperature, and concentration distributions of THSN were examined meticulously in this section as well as the physical significance of the relevant physical parameters that have an immediate impact on those distributions. The following ranges of the pertinent parameters are considered in the current investigation as (see Refs. [40-44]):

$$-1 \le E_1 \le 1, \ 0 \le M \le 3, \ -5 \le m \le 5, \ 0 \le De \le 7, \ 0 \le k_1^* \le 5, \ 0 \le \chi \le 2, \ 0.1 \le N \le 3, \ 0 \le Rd \le 5, \ 0.1 \le Ec \le 0.8,$$

$$0.1 \le (Nt, Nb) \le 2, \ 0.1 \le Sc \le 2, \ 0 \le (\delta_1, \delta_2, \delta_3) \le 1, -3 \le (\gamma_1, \gamma_2, \gamma_3) \le 0.$$

We employed Tables 3 and 4 to scrutinize the same parameters on C_{fx}, Nu_x, and Sh_x.

Table 2. Comparing of $-F''(0)$ and $-\Theta'(0)$ in a viscous Newtonian fluid for different values of Γ, χ, M, n, and Pr.

Γ	χ	M	n	Pr	Vajravelu et al. [41]		Present work	
					$-F''(0)$	$-\Theta'(0)$	$-F''(0)$	$-\Theta'(0)$
0.5	0.5	1.0	2.0	0.71	1.2024	0.9763	1.2069	0.976883
1.0					1.1322	0.9304	1.13272	0.930886
	1.0				0.9481	0.9762	0.948405	0.977841
		2.0			1.2738	0.90604	1.27677	0.908137
			5.0		1.2398	1.0402	1.2395	1.04525
				7.0	1.3567	2.7146	1.35661	2.71441

Table 3. Computed values of $C_{fx}Re_x^{1/2}$, $Nu_xRe_x^{-1/2}$, and $Sh_xRe_x^{-1/2}$ for dissimilar values of flow parameters E_1, M, k_1^*, m, De, χ, Rd, Sc, and Ec.

E_1	M	k_1^*	m	De	χ	Rd	Sc	Ec	$C_{fx}Re_x^{1/2}$	$Nu_xRe_x^{-1/2}$	$Sh_xRe_x^{-1/2}$
-0.5									-0.67889	0.335938	0.256758
0									-0.510547	0.368315	0.291722
1									-0.126334	0.97508	0.465156
	0.1								-0.438791	0.316999	0.280233
	0.6								-0.578978	0.326825	0.274826
	2								-0.630401	0.347178	0.255429
		0							-0.623858	0.323876	0.263247
		0.3							-0.613579	0.327208	0.266604
		1							-0.578181	0.331739	0.268623
			-5						-1.00917	0.352777	0.285023
			0						-0.652738	0.343168	0.275901
			5						-0.416907	0.33356	0.266779
				0					-0.641624	0.328413	0.267631
				2					-0.573941	0.325401	0.265063
				5					-0.486868	0.320883	0.261213
					0.5				-0.572805	0.341644	0.283696
					1				-0.469267	0.377732	0.326426
					1.5				-0.363792	0.413821	0.369156
						0			-0.612527	0.253615	0.269569
						1			-0.614858	0.499245	0.262999
						3			-0.616098	0.991433	0.259503
							0.5		-0.613935	0.326584	0.273423
							1		-0.614823	0.325022	0.291957
							1.5		-0.615712	0.323461	0.312611
								1	-0.605224	0.382696	0.290938
								3	-0.58126	0.541234	0.360466
								5	-0.557162	0.699772	0.429994

Table 4. Computed values of $C_{fx}Re_x^{1/2}$, $Nu_xRe_x^{-1/2}$, and $Sh_xRe_x^{-1/2}$ for dissimilar values of flow parameters Nb, Nt, δ_1, δ_2, δ_3, γ_1, γ_2, and γ_3.

Nb	Nt	δ_1	δ_2	δ_3	γ_1	γ_2	γ_3	$C_{fx}Re_x^{1/2}$	$Nu_xRe_x^{-1/2}$	$Sh_xRe_x^{-1/2}$
0.3								-0.680078	0.337461	0.272517
1								-0.677306	0.33412	0.250454
1.5								-0.675325	0.332192	0.247303
	0.3							-0.613982	0.327309	0.262879
	1							-0.611161	0.323343	0.303483
	1.5							-0.609145	0.315856	0.353242
		0						-0.711681	0.32481	0.266161
		0.4						-0.585212	0.327718	0.266517
		1						-0.453756	0.32934	0.265303
			0					-0.609529	0.351816	0.269033
			0.4					-0.614798	0.31983	0.265888
			1					-0.621019	0.282225	0.262346
				0				-0.612921	0.326762	0.290598
				0.4				-0.613775	0.327332	0.259471
				1				-0.614756	0.327895	0.223641
					-3			-0.231658	0.332282	0.262042
					-1			-0.441076	0.329463	0.265072
					-0.5			-0.613579	0.327208	0.266604
						-3		-0.606945	0.326677	0.266604
						-1		-0.612253	0.328067	0.266604
						-0.5		-0.613579	0.327208	0.266604
							-3	-0.613754	0.328043	0.246372
							-1	-0.613614	0.327375	0.262534
							-0.5	-0.613579	0.327208	0.266604

Figures 2(a)-(c) elucidate the behavior of E_1 on the velocity profile. The velocity growths as the intensity of E_1 rises. This is due to an enormous amount of electric field causing accelerated ionization in THSN, which boosts the motion of nanoparticles. The momentum boundary layer (MBL) thickness upsurges along with the electric field's strength. The temperature sketches are revealed in Fig. 2(b) exhibiting the reverse behavior. Figure 2(c) displays that the concentration upsurges with the growth of M. It is evident from Figs. 2(d)-(f) that for increased values of M, the velocity and MBL thickness lessened. Because the perpendicularly applied magnetic field generates the Lorentz force, which contradicts the fluid's flow. This results in the greatest Lorentz force. The Lorentz force is created when magnetic and electric fields interrelate whilst a fluid having electrical conductivity is moving. As the magnetic field strength rises, the thermal boundary layer (TBL) thickness also does. The concentration is diminution with the enhancement in M.
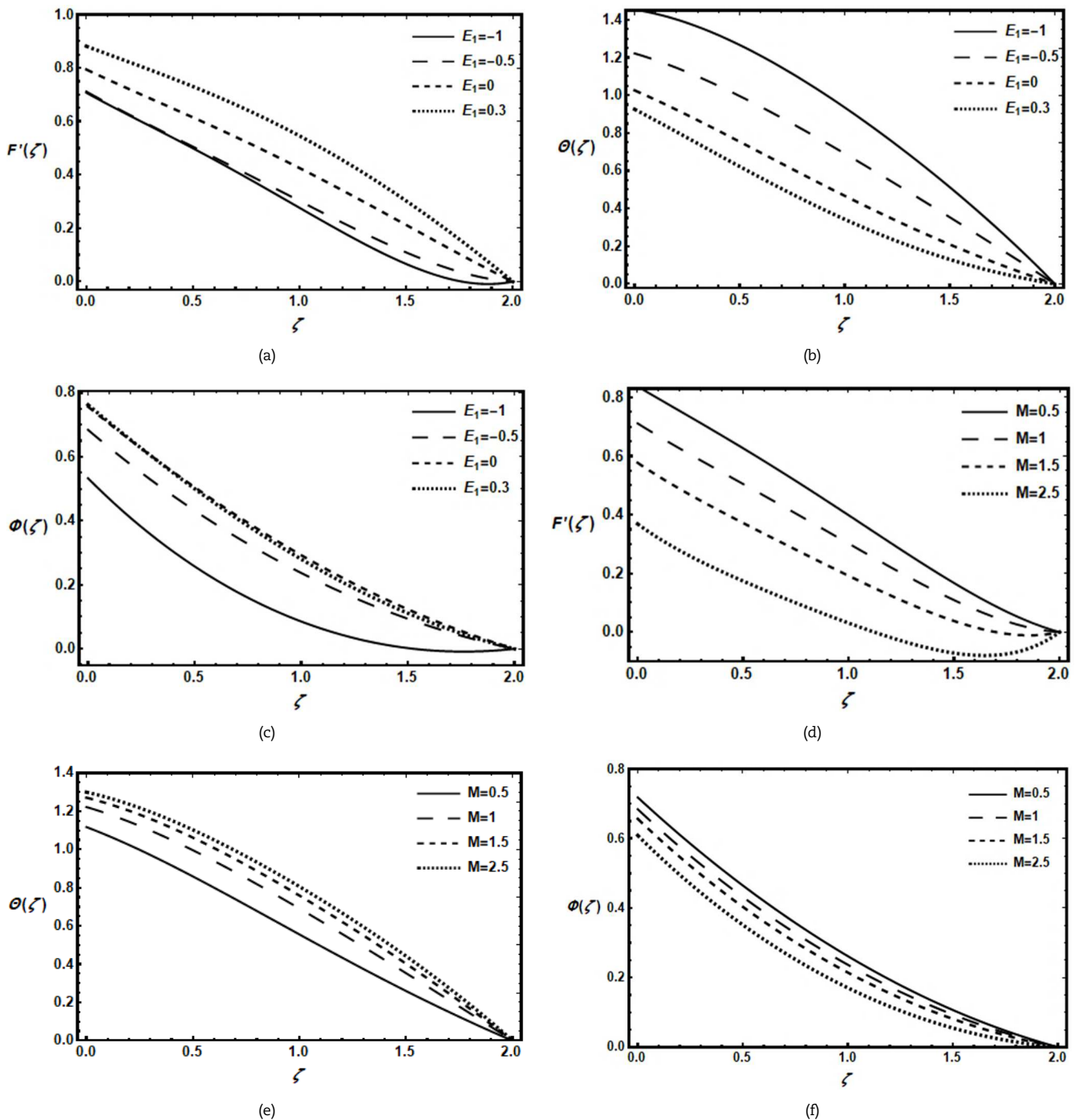
(a)

(b)

(c)

(d)

(e)

(f)

Fig. 2. Variation of electric and magnetic field parameters via velocity, temperature, and concentration profiles.

The influence of k_1^* on the velocity, temperature, and concentration outlines have appeared in Figs. 3(a)-(c). It has been found that an increase in k_1^* causes the velocity to decrease. Physically, the permeability of the medium's porous structure causes an increase in resistance, which lowers the fluid velocity. This happens as a result of the porosity parameter increasing, the punctures in porous layers enlarge and decline MBL thickness. internal thermal energy is created and discharged to the flow when the porosity parameter increases. As a result, we noticed that the profiles of temperatures boosted far away the surface of stretching sheet. The porous medium parameter k_1^* assists in improving the temperature as well as concentration boundary layer (CBL) thickness. Figure 3(d) indicates that a growth in N leads to an upsurge in fluid velocity. N is known to be the proportion of buoyancy force via inertia force. When The buoyancy force is greater than the inertia force, N becomes larger. As a result, an increment in N gives rise to a faster flow of fluid in the region. Conversely, the concentration distribution and far off the surface of stretching sheet the temperature distribution, as demonstrated in Figs. 3(e) and 3(f), show the opposite trend.

The Rd of velocity, temperature distribution, and field of concentration have been shown in Figs. 4(a)-(c). It is perceived from Figs. 4(a) and (c) that Rd decreases the velocity profiles when it is increased, and the opposite outcome of Rd is noticed for the concentration field. Controlling the temperature of a fluid can be achieved through thermal radiation. This is because the temperature is highly affected by thermal radiation, resulting in a higher heat flux at the surface. The TBL thickness will also increase as the thermal radiation enlarges. Thus, the temperature is nourishing as demonstrated in Fig. 4(b). Degeneracy is exemplified by the Eckert number Ec, which shows how the kinetic energy and flow's enthalpy relate to one another. In Figs. 4(d)–

4(f), the influence of Ec on velocity, temperature, and concentration distributions is depicted. The increment of Ec influenced the velocity and temperature curves to upsurge. The drag forces among the molecules of a liquid increase as Ec increases. The result is an increase in energy production, which improves THN thermal profile. Also, change in Ec due to dwindling on concentration.

The effect of Nt on velocity and concentration distributions is illustrated in Figs. 5(a)-(b). As the value of Nt increases, so do the velocity distribution. This is owing to the positive quantities of the thermophoretic parameter, which mainspring the fluid flow to movement from the hot surface toward the cold surface. Therefore, it can be concluded that the application of the thermophoretic parameter to the fluid flow promotes TBL thickness. Furthermore, a rise in Nt causes to the coefficient of thermophoretic diffusion, which declines the mass concentration as shown in Fig. 5(b). The velocity nanofluid and concentration field were influenced by the Brownian motion parameter Nb, as seen in Figs. 5(c)-(d). Figure 5(c) confirms that a higher Nb causes the velocity profile to boost. That's because an upsurge in the temperature field and correlated layer thickness within the Nb frame. A higher Nb causes liquid particles to move more, producing more heat. As a result of the liquid particles' random motion, more heat is consequently supplied. Figure 5(d) shows that an increase in Nb makes CBL thickness rises. This is because as Nb increases; particle deposition gets more extreme far from the fluidity regime and closer to the surface.
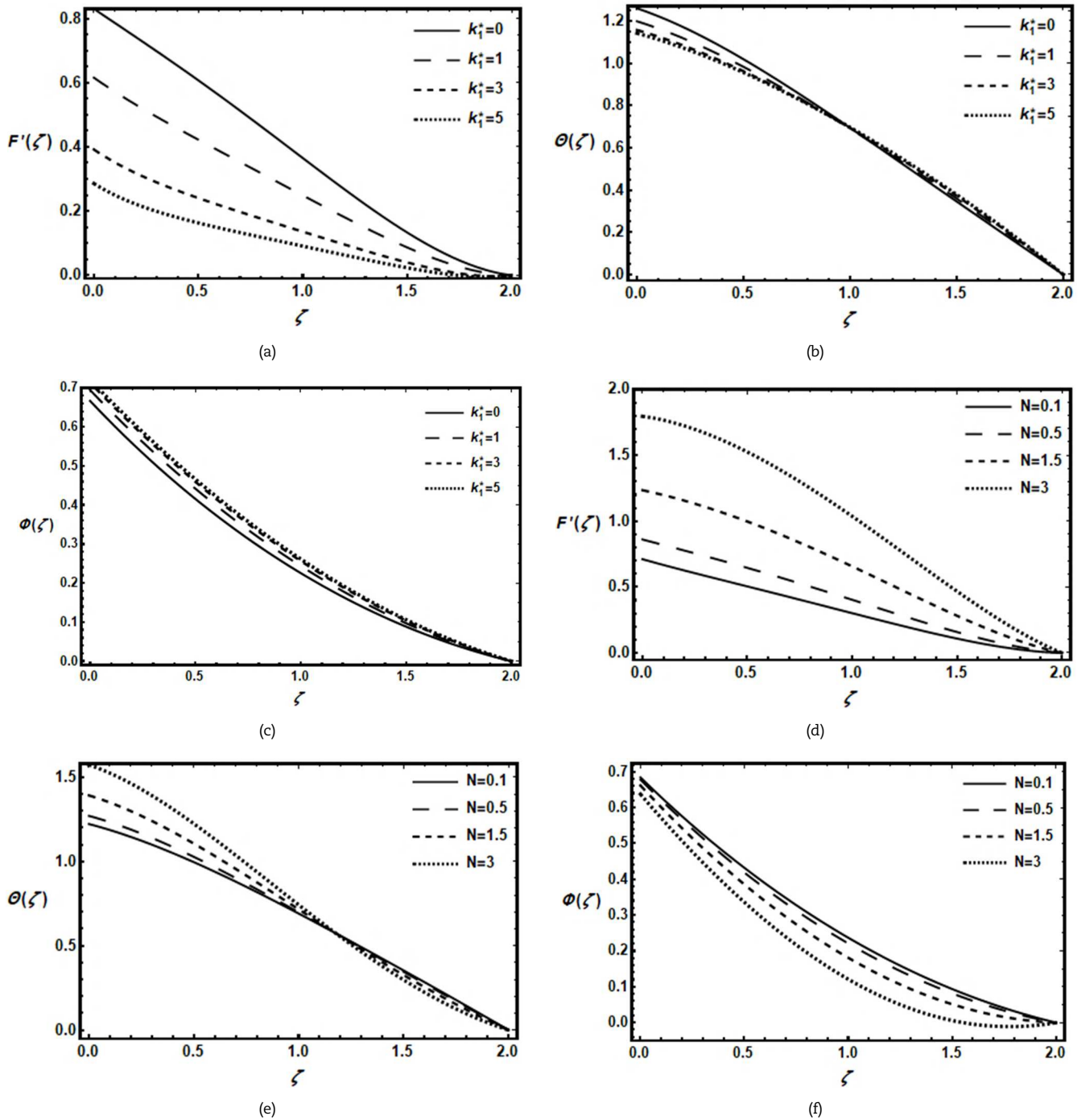

(a)

(b)

(c)

(d)

(e)

(f)

Fig. 3. Variation of the porous medium and mixed convection flow parameters via velocity, temperature, and concentration profiles.

(a)

(b)

(c)

(d)
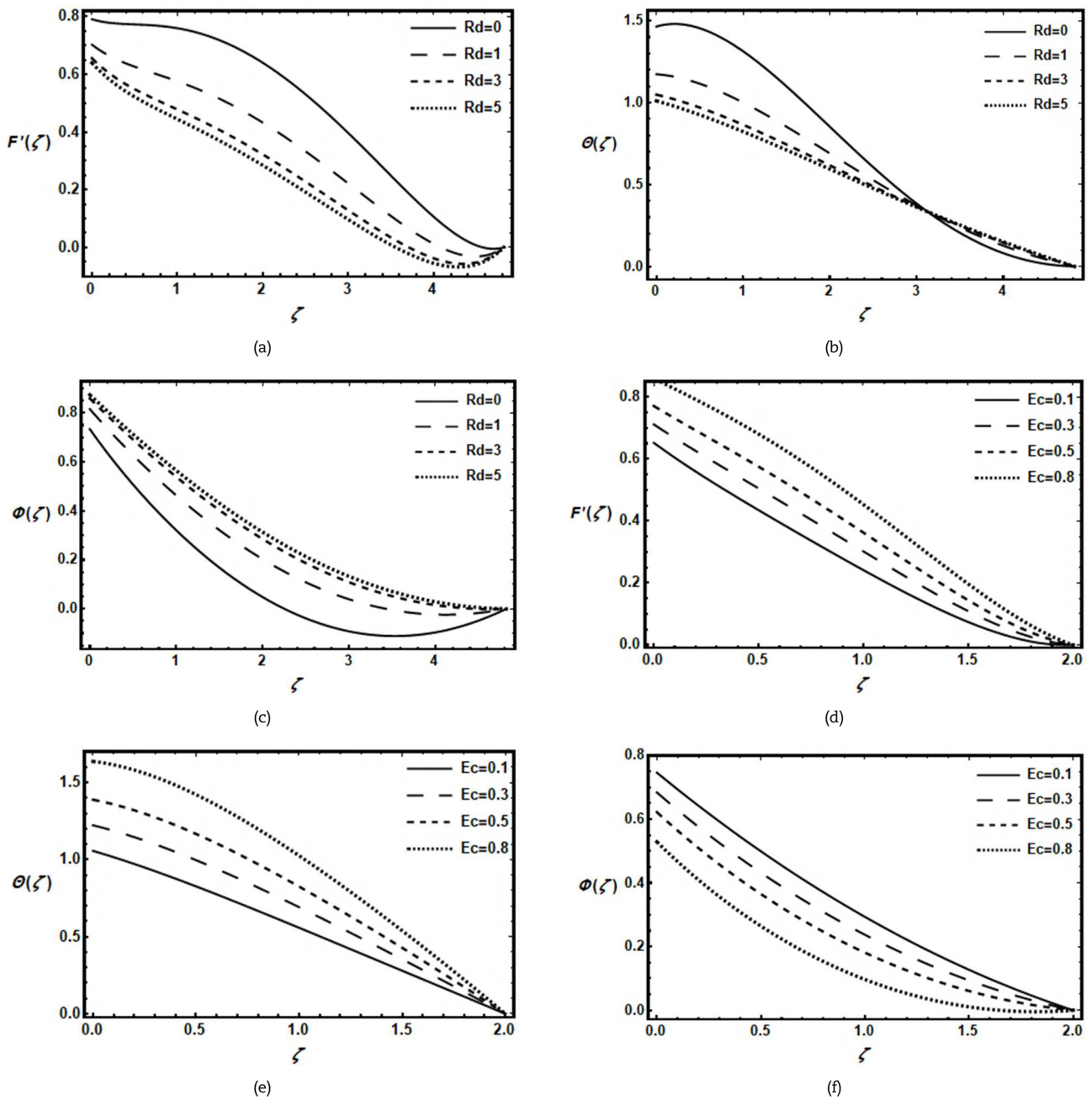
(e)

(f)

Fig. 4. Variation of thermal radiation and Eckert number parameters via velocity, temperature, and concentration profiles.
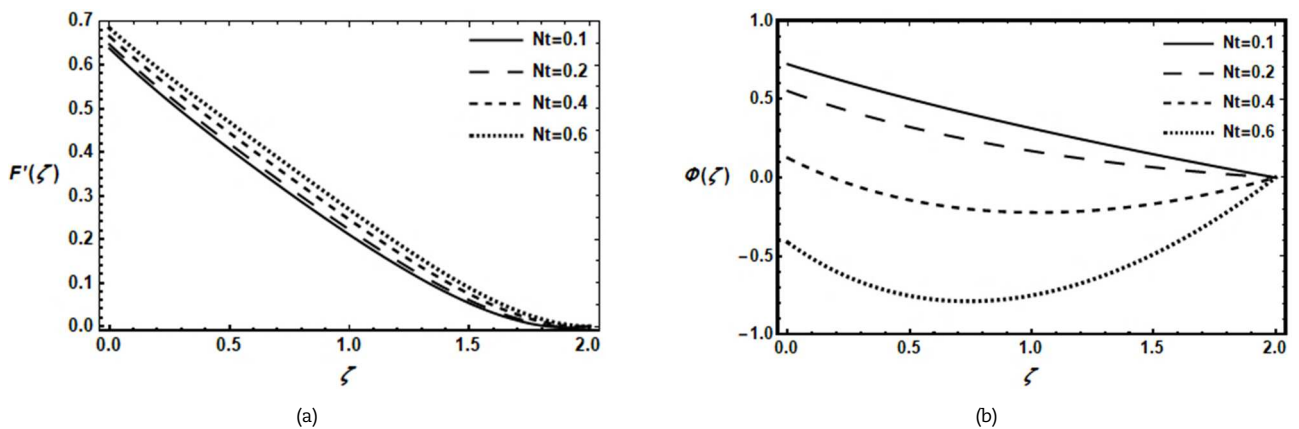
(a)

(b)

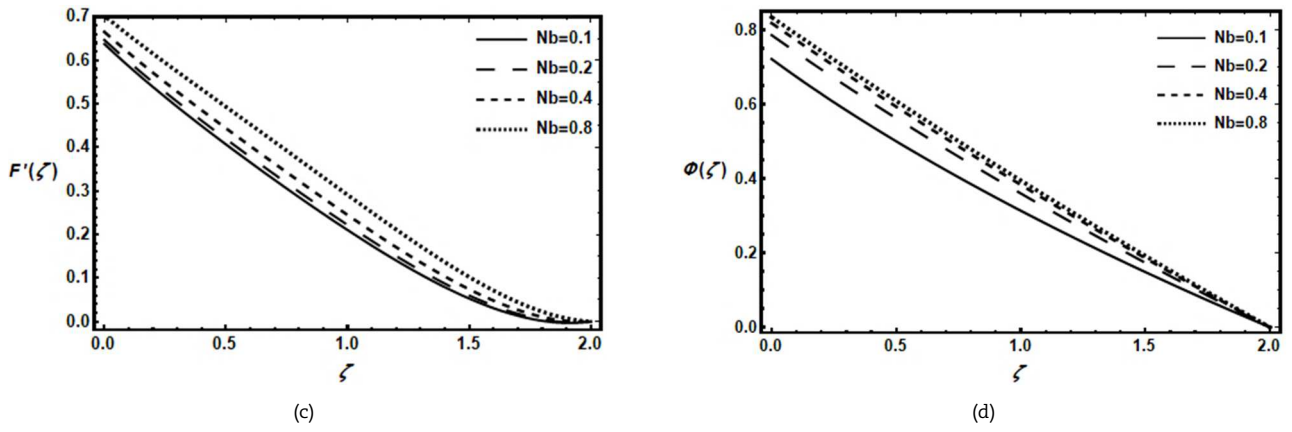**Fig. 5.** Variation of thermophoresis and Brownian motion parameters via velocity, temperature, and concentration profiles.
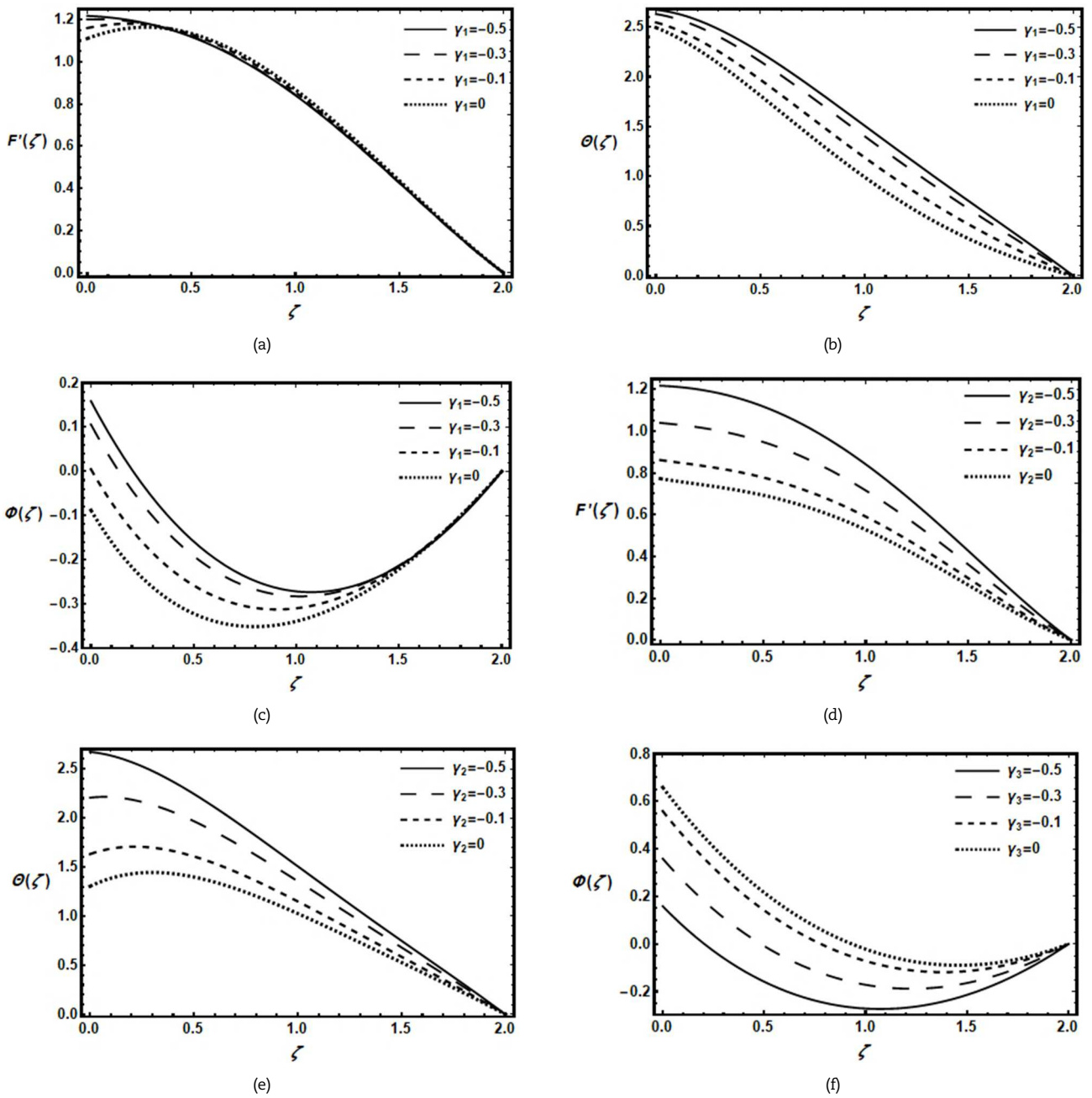
(c)

(d)

Fig. 5. Continued.

(a)

(b)

(c)

(d)

(e)

(f)

Fig. 6. Variation of second-order velocity, thermal, and concentration slip parameters via velocity, temperature, and concentration profiles.

Illustrations in Figs. 6(a)-(c) demonstrate the effect of γ_1 on the profiles of velocity, temperature, and concentration. As the absolute value of γ_1 decreases near the surface sheet, velocity gradually increases, whereas it behaves the opposite away from the wall. Conversely, the concentration field behaves oppositely. Additionally, an increase in γ_1 produces an upsurge in both TBL thickness and the temperature distribution. The velocity and temperature distributions are presented in Figs. 6(d)-(e) to show the impact of the second-order thermal slip parameter, γ_2. As evidenced by these Figs., Increasing γ_2 causes the thickness of both MBL and TBL to decline. Also, the concentration profile diminishes. Figure 6(f) displays the variations of the concentration with the second-order concentration slip parameter γ_3. We can reveal that, when γ_3 increases the concentration profile increases. Additionally, we noticed a decline in the temperature and velocity profiles.

Figsures 7(a)-(c) clarify the impact of Pr on the velocity, temperature, and concentration profiles. The MBL thickness grows as Pr enhances, which also induces an elevation in the velocity profile. The temperature profile and TBL thickness rise with increasing Pr, as shown in Figs. 7(a)-(b). Physical manifestation Pr is the proportion of momentum diffusivity to thermal diffusivity. The Pr regulates the relative thickness of MBL and TBL in the heat transmission problem. A high Pr causes heat to diffuse rapidly than velocity, hence for metallic liquid, TBL is substantially thicker than MBL. Greater Pr values in fluids result in thicker TBL, which allow heat to navigate the sheet more quickly than in lower Pr fluids. Consequently, one could be using Pr to accelerate the cooling process. A lower concentration is observed as Pr increases (Fig. 7(c)). Figures 7(d)-(f) display the velocity, temperature, and concentration distributions for several fluids: the base fluid ($\varphi_1 = 0, \varphi_2 = 0, \varphi_3 = 0$), nanofluid ($\varphi_1 = 0, \varphi_2 = 0, \varphi_3 = 0.03$), hybrid nanofluid ($\varphi_1 = 0.03, \varphi_2 = 0, \varphi_3 = 0.03$), and THN ($\varphi_1 = 0.03, \varphi_2 = 0.03, \varphi_3 = 0.03$). In Fig. 7(d), compared to pure fluid, mono-nanofluids, and bi-nanofluid, the THN illustrates less motion. The THN demonstrates the lowliest heat compared to the bi-nanofluid, mono-nanofluid, and base fluid. This suggests that the THN possesses superior thermal conductivity in comparison to the other fluids. The reason behind this is that an increased volume fraction of nanoparticles facilitates faster heat transmission from the surface of the thin cylinder's surface to the fluid's surrounding. Consequently, the thermal conductivity of the THN escalates, resulting in a significant decline in the temperature field, as revealed in Fig. 7(e). Moreover, In Fig. 7(f), it can be observed that the concentration boundary layer created by the tri-hybrid nanoparticles is greater in comparison to the concentration boundary layer formed by mono-nanoparticles and bi-nanoparticles.

The impression of some physical parameters on $C_{fx}Re_x^{1/2}$, $Nu_xRe_x^{-1/2}$ as well as $Sh_xRe_x^{-1/2}$ is scrutinized using Tables 3 and 4. Finding indicate that augmenting values of $E_1, k_1^*, m, De, \chi, Ec, Nb, Nt, \delta_1$ and γ_3 maximizes the skin friction coefficient but the opposite performance occurs with the rising values of $M, Rd, Sc, \delta_2, \delta_3, \gamma_1$ and γ_2. The local Nusselt number minimizes as $m, De, Sc, Nb, Nt, \delta_2, \gamma_2$ and γ_3 boost, while its growth with increasing $E_1, M, k_1^*, \chi, Rd, Ec, \delta_1, \delta_3$ and γ_1. A strength in $E_1, k_1^*, \chi, Ec, Sc, Nt, \gamma_1$ and γ_3 cause a intensify in Sherwood number. On the other hand, as $M, m, De, Rd, Nb, \delta_1, \delta_2$ and δ_3 values rise, the Sherwood number diminishes.

6. Conclusions

The investigation focused on analyzing the behavior of a THSN exposed to EMHD radiation flow. The nanofluid flowed over a nonlinear stretching surface beside varying thickness inside of porous medium and second-slip conditions. To simplify the mathematic PDEs, similarity variables were employed, and the results were obtained through the utilization of the HPM.
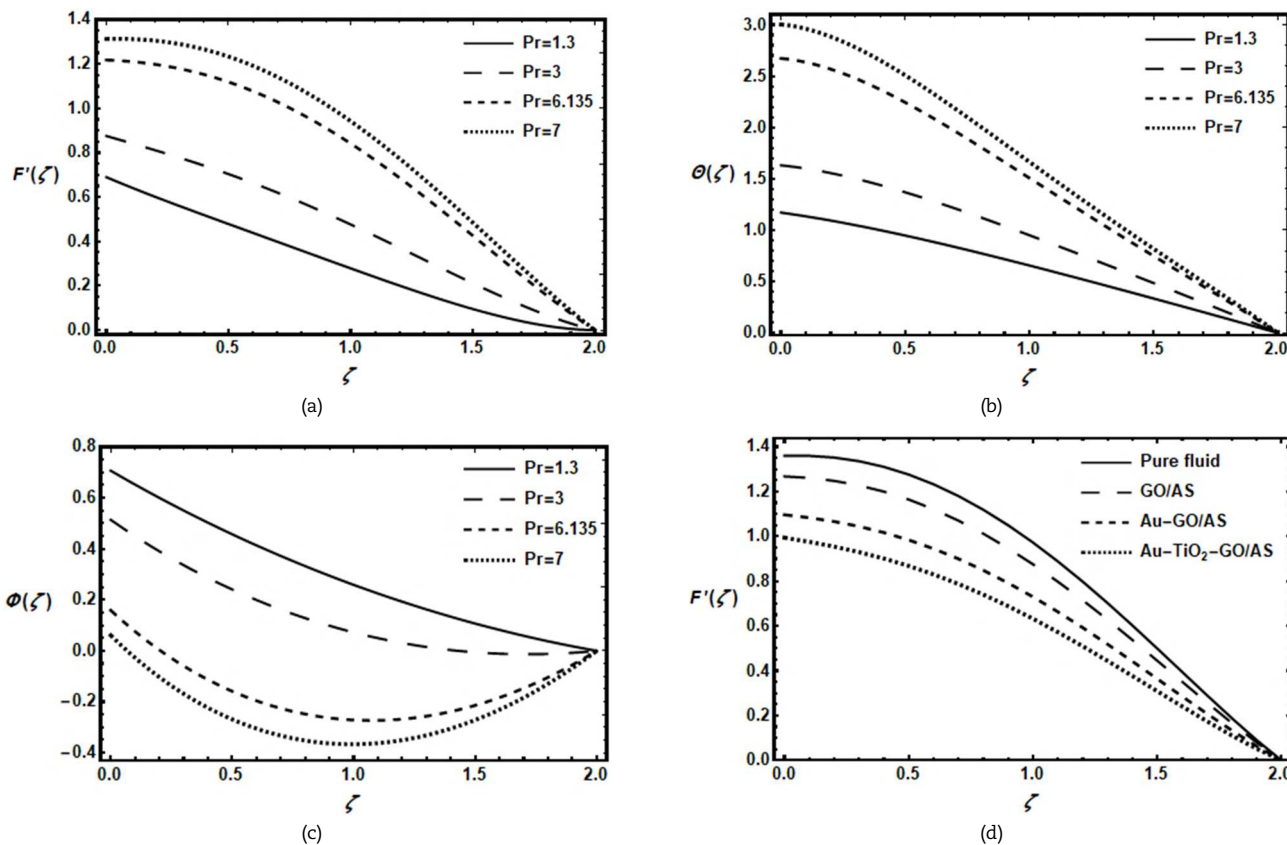

Fig. 7. Variation of Prandtl number and volume ratio of solid nanoparticles via velocity, temperature, and concentration profiles.
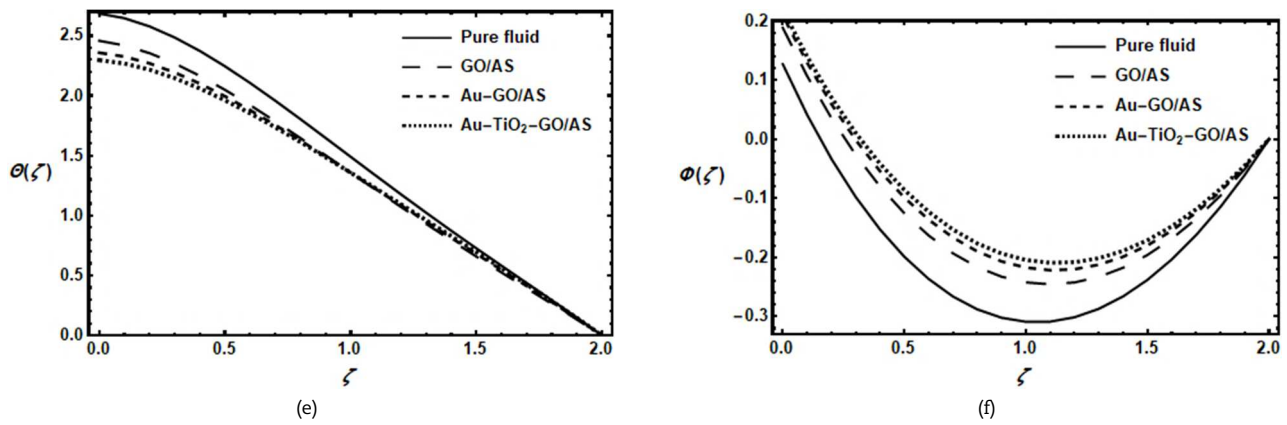
Fig. 7. Continued.

The study concludes that:

1. The velocity field rises with intensifying the electric field parameter, Eckert number, mixed convection flow parameter, thermophoresis parameter, Brownian motion parameter, and second-order velocity slip parameter away from the wall and falls with growing the magnetic field parameter, thermal radiation parameter, porous medium parameter, and parameters of second-order temperature jump and second-order velocity slip near the surface sheet.

2. The thermal distribution shows an increasing trend for the Eckert number, porous medium parameter away from the wall, and magnetic field parameter while reducing for enlarging the value of electric field parameter, mixed convection flow parameter away from the wall, thermal radiation parameter near the surface sheet, second-order temperature jump and second-order velocity slip parameters.

3. The concentration distributions experience a decrease in their magnitude owing to the impact of various parameters, including the magnetic field parameter, mixed convection flow parameter, thermophoresis parameter, Eckert number, second-order slip parameter for velocity, and second-order jump parameter for concentration, while increased for higher electric field parameter, porous medium parameter, Brownian motion parameter, and thermal radiation parameter.

4. Thick thermal boundary layer in fluid with higher Pr values facilitate faster heat transfer through the sheet than in fluid with lower Pr values.

5. The fluidic motion of ternary hybrid nanoparticles exhibits a lower magnitude compared to that of bi-nanofluid, mono-nanofluid, and pure fluid.

6. Compared to the bi-nanofluid, mono-nanofluid, and base fluid, THN exhibits the lowest temperature.

7. Higher concentration profiles are observed in THN when compared to the bi- nanofluid, mono-nanofluid, and pure fluid.

8. Skin friction coefficients are escalating function of E_1, m, De, δ_1 and γ_3 while they are decreasing with δ_2, δ_3, γ_1 and γ_2. Local Nusselt number is growing for larger of E_1, δ_1, δ_3 and γ_1 while it shows shrinking behavior with m, De, δ_2, γ_2 and γ_3. Sherwood number is rising via augmented E_1, γ_1 and γ_3 and reducing by m, De, δ_1, δ_2 and δ_3.

Benefiting from EMHD radiation and multi-slip conditions, the study offers important insights into how different parameters affect a trihybrid nanofluid flow's thermal behavior. The results have applications in engineering where they can be utilized to upgrade the performance and design of heat transmission systems in various industries such as melt-spinning, rubber and plastic sheet manufacture, extrusion, metallic plate cooling in a bath, petroleum production, polymer sheet extraction, glass-fiber manufacturing, and wire drawing.

Author Contributions

G.M. Moatimid and H.M. Sayed were instrumental in the research conceptualization, developing the research methodology, analyzing the results, and writing the manuscript.

Data Availability Statements

The datasets generated and/or analyzed during the current study are available from the corresponding author on reasonable request.

Nomenclature

List of symbols

U_0	Rate of reference stretching (ms^{-1})
n	Stretching index
d	Dimensionless constant
$B(x)$	non-uniform magnetic strength (Tesla)
$E(x)$	Variable electric field (Vm^{-1})
$K(x)$	Variable permeability (m²)
τ	Trihybrid nanofluid temperature (K)
T_w	Temperature at slender sheet surface (K)
T_∞	Ambient temperature (K)
C	Trihybrid nanofluid concentration (kgm^{-2})
C_w	Nanoparticle concentration at slender sheet surface (kgm^{-2})
C_∞	Ambient concentration (kgm^{-2})
m	Power law index
b	Material constant (kgm^{-1})
u,v	Components of velocity along the axial and transverse directions (ms^{-1})
k	Thermal conductivity ($Wm^{-1}K^{-1}$)
E_0	Intensity of the electric field
B_0	Flux density of the applied magnetic field
k_0	Permeability of the absorbent
g	Gravitational force (ms^{-2})
σ_e	Stefan-Boltzmann constant
β_R	Coefficient of mean absorption
τ	Effective heat capacitance
D_B	Brownian coefficient (m^2s^{-1})
D_T	Thermophoretic diffusion coefficient (m^2s^{-1})
ρC_p	Effective heat capacity ($Jkg^{-3}m^{-1}$)
k_1,k_2,k_3	First-order velocity slip, temperature jump, and concentration jump parameters
J_1,J_2,J_3	Second-order velocity slip, temperature jump, and concentration jump parameters
De	Deborah number
k_1^*	Porous medium parameter
E_1	Electric field parameter
M	Magnetic field parameter
Gr_T	Local thermal Grashof number
Gr_C	Mass diffusion Grashof number
N	Mixed convection flow parameter
Re_x	Local Reynolds number
Rd	Thermal radiation parameter
Pr	Prandtl number
Ec	Eckert number
Nt	Thermophoresis parameter
Nb	Brownian motion parameter
Sc	Schmidt number
q	homotopy parameter

Greek symbols

δ	Sheet thin parameter
ρ	Density (kgm^{-3})
μ	Dynamic viscosity (Pa.S)
ν	Kinematic viscosity (m^2s^{-1})
σ	Electrical conductivity ($\Omega^{-1}m^{-1}$)
β_T	Heat flux expansion coefficient (K^{-1})
β_C	Mass flux expansion coefficient (K^{-1})
β_1,β_2,β_3	Maxwall's coefficients for reflection, thermal accommodation, and concentration accommodation
η_1,η_2,η_3	Mean free path constants
λ	Ratio of specific heats
$\varphi_1,\varphi_2,\varphi_3$	Volume ratio of solid nanoparticles
$\delta_1,\delta_2,\delta_3$	Dimensionless first-order velocity slip, temperature jump, and concentration jump parameters
$\gamma_1,\gamma_2,\gamma_3$	Dimensionless second-order velocity slip, temperature jump, and concentration jump parameters
Γ	Wall thickness parameter
χ	Buoyancy parameter

Subscripts

tnf	Trihybrid nanofluid
hnf	Binary nanofluid
nf	Unary nanofluid
f	Base fluid
w	Surface condition
∞	Free stream condition

Superscript

'	Differentiation with respect to ξ

References

[1] Waqas, H., Farooq, U., Muhammad, T., Hussain, S, Khan, I., Thermal effect on bioconvection flow of Sutterby fluid between two rotating disks with motile microorganisms, *Case Studies in Thermal Engineering*, 26, 2021, 101136.

[2] Yahya, A.U., Salamat, N., Habib, D., Ali, B., Hussain, S., Abdal, S., Implication of bio-convection and Cattaneo-Christov heat flux on Williamson Sutterby nanofluid transportation caused by a stretching surface with convective boundary, *Chinese Journal of Physics*, 73, 2021, 706–718.

[3] Fayyadh, M.M., Naganthran, K., Basir, M.F.M., Hashim, I., Roslan, R., Raiative MHD Sutterby nanofluid flow past a moving sheet: scaling group analysis, *Mathematics*, 8, 2020, 1430.

[4] Gowda, R.J.P., Kumar, R.N., Rauf, A., Prasannakumara, B.C., Shehzad, S.A., Magnetized flow of Sutterby nanofluid through Cattneo-Christov theory of heat diffusion and Stefan blowing condition, *Applied Nanoscience*, 13, 2023, 585–594.

[5] Aldabesh, A., Haredy, A., Al-Khaled, K., Khan, S.U., Tlili, I., Darcy resistance flow of Sutterby nanofluid with microorganisms with applications of nano-biofuel cells, *Scientific Reports*, 12, 2022, 7514.

[6] Moatimid, G.M., Mohamed, M.A.A., Elagamy, Kh., Sutterby nanofluid flow with microorganisms around a curved expanding surface through a porous medium: Thermal diffusion and diffusion thermo impacts, *Journal of Porous Media*, 27, 2024, 19-48.

[7] Moatimid, G.M., Elgazery, N. S., Mohamed, M.A.A., Elagamy, Kh., Bio-Convection flow of Sutterby nanofluid with motile microbes on stretchable sheet: Exponentially varying viscosity, *Journal of Applied and Computational Mechanics*, 10(3), 2024, 488-502.

[8] Khan, M.I., Waqas, H., Farooq, U., Khan, S.U., Chu, Y.M., Kadry, S., Assessment of bioconvection in magnetized Sutterby nanofluid configured by a rotating disk: A Numerical Approach, *Modern Physics Letters B*, 35, 2021, 2150202.

[9] Sohail, M., Naz, R., Modified Heat and mass transmission models in the magnetohydrodynamic flow of Sutterby fluid flow in stretching cylinder, *Physica A: Statistical Mechanics and its Applications*, 549, 2020, 124088.

[10] Baithalu, R., Mishra, S.R., Pattnaik, P.K., Panda, S., Optimizing shear and couple stress analysis for the magneto-micropolar dissipative nanofluid flow toward an elongating surface: A comprehensive RSM-ANOVA investigation, *Journal of Thermal Analysis and Calorimetry*, 149, 2024, 1697–1713.

[11] Shaoa, W., Baithalu, R., Mishra, S.R., Dogonchi, A.S., Ali R., Chamkha, A.J., Galal, A.M., Statistical approach on optimizing heat transfer rate for Au/Fe₃O₄- blood nanofluid flow with entropy analysis used in drug delivery system, *Case Studies in Thermal Engineering*, 54, 2024, 104008.

[12] Ali, F., Loganathan, K., Prabu, E., Eswaramoorthi, S., Faizan, M., Zaib, A., Chaudhary, D.K., Entropy minimization on Sutterby nanofluid past a stretching surface with swimming of gyrotactic microorganisms and nanoparticles, *Mathematical Problems in Engineering*, 2021, 2021, 5759671.

[13] Baithalu, R., Mishra, S.R., Shah, N.A., Sensitivity analysis of various factors on the micropolar hybrid nanofluid flow with optimized heat transfer rate using response surface methodology: Statistical approach, *Physics of Fluids*, 35, 2023, 102016.

[14] El-Dabe, N.T.M., Moatimid, G.M., Mohamed, M.A.A., Mohamed, Y.M., A couple stress of peristaltic motion of Sutterby micropolar nanofluid inside a symmetric channel with a strong magnetic field and Hall currents effect, *Archive of Applied Mechanics*, 91, 2021, 3987–4010.

[15] Ali, e.B., Sharif, H., Habib, D., Ghazwani, H.A., Saman, I., Yang, H., Significance of tri-hybrid nanoparticles in thermal management subject to magnetized squeezing flow of a Boger-micropolar nanofluid between concentering disks, *Journal of Molecular Liquids*, 397(3), 2024, 124141.

[16] Raza, Q., Wang, X., Ali, B., Eldin, S.M., Yang H., Siddique, I., Role of nanolayer on the dynamics of tri-hybrid nanofluid subject to gyrotactic microorganisms and nanoparticles morphology via two porous disks, *Case Studies in Thermal Engineering*, 51, 2023, 103534.

[17] Shinwari, W., Hayat, T., Abbas, Z., Momani, S., Numerical study for trihybrid nanomaterial flow by convectively heated curved sheet, *Case Studies in Thermal Engineering*, 53, 2024, 103962.

[18] Hou, E., Wang, F., Nazir, U., Sohail, M., Jabbar, N., Thounthong, P., Dynamics of tri-hybrid nanoparticles in the rheology of pseudo-plastic liquid with Dufour and Soret effects, *Micromachines*, 13(2), 2022, 201.

[19] Yang, D., Ahmad, S., Ali, K., Algarni, S., Alqahtani, T., Jamshed W., Hussain, S.M., Irshad, K., and Ahmad, H., CFD analysis of paraffin-based hybrid (Co–Au) and trihybrid (Co–Au–ZrO₂) nanofluid flow through a porous medium, *Nanotechnology Reviews*, 13, 2024, 20240024.

[20] Arif, M., Persio L.D., Kumam, P., Watthayu W., Akgül A., Heat transfer analysis of fractional model of couple stress Casson tri-hybrid nanofluid using dissimilar shape nanoparticles in blood with biomedical applications, *Scientific Reports*, 13, 2023, 4596.

[21] Baithalu, R., Mishra, S.R., On Optimizing Shear Rate Analysis for the water-based CNT micropolar nanofluids via an elongating surface: Response surface methodology combined with ANOVA test, *Journal of Thermal Analysis and Calorimetry*, 148, 2023, 14275–14294.

[22] Panda, S., Baag, A.P., Pattnaik, P.K., Baithalu, R., Mishra S.R., Artificial neural network approach to simulate the impact of concentration in optimizing heat transfer rate on water-based hybrid nanofluid under slip conditions: A regression analysis, *Numerical Heat Transfer, Part B: Fundamentals*, 2024, 1-23. https://doi.org/10.1080/10407790.2024.2333944.

[23] Sagheera, S., Razzaq, R., Vafaia, K., Local non-similar solutions for EMHD nanofluid flow with radiation and variable heat flux along slandering stretching sheet, *Numerical Heat Transfer, Part B: Fundamentals*, 2024. https://doi.org/10.1080/10407782.2024.2360082.

[24] Bhatti, M.M., Bég, O.A., Ellahi, R., Doranehgard, M.H., Rabiei, F., Electro-magnetohydrodynamic hybrid nanofluid flow with gold and magnesium oxide nanoparticles through vertical parallel plates, *Journal of Magnetism and Magnetic Materials*, 564, 2022, 170136.

[25] Kanwal, A., Khan A.A., Sait, S.M., Ellahi, R., Heat transfer analysis of magnetohydrodynamics peristaltic fluid with inhomogeneous solid particles and variable thermal conductivity through curved passageway, *International Journal of Numerical Methods for Heat & Fluid Flow*, 34(4), 2024, 1884-1902.

[26] Bau, H.H., Applications of magneto electrochemistry and magnetohydrodynamics in microfluidics, *Magnetochemistry*, 8(11), 2022, 140.

[27] Kiamari, M., Sadooghi N., Jafari M.S., Relativistic magnetohydrodynamics of a spinful and vortical fluid: Entropy current analysis, *Physical Review D*, 109, 2024, 036024.

[28] Kundu, B., Saha, S., Review and analysis of electro-magnetohydrodynamic flow and heat transport in microchannels, *Energies*, 15, 2022, 7017.

[29] He, J-H., Homotopy perturbation technique, *Computer Methods in Applied Mechanics and Engineering*, 178(3), 1999, 257-262.

[30] He, J-H., A coupling method of a homotopy technique and a perturbation technique for non-linear problems, *International Journal of Non-Linear Mechanics*, 35(1), 2000, 37-43.

[31] He, J-H., Homotopy perturbation method: A new nonlinear analytical technique, *Computational and Applied Mathematics*, 135(1), 2003, 73-79.

[32] He J-H., Moatimid G.M., Mohamed, M.A.A., Elagamy, Kh., Unsteady MHD flow in a rotating annular region with homogeneous–heterogeneous chemical reactions of Walters' B fluids: Time-periodic boundary criteria, *International Journal of Modern Physics B*, 38(14), 2024, 2450169.

[33] Moatimid, G.M., Mohamed, M.A.A., and Elagamy, Kh., Microorganisms peristaltic transport within a Carreau nanofluid through a modified Darcy porous medium, *Special Topics and Reviews in Porous Media*, 14(5), 2023, 1-30.

[34] Moatimid, G.M., Mohamed, M.A.A., and Elagamy, Kh., A Williamson nanofluid with motile microorganisms across a vertical exponentially stretching porous sheet with varying thermal characteristics, *Special Topics and Reviews in Porous Media*, 15(1), 2024, 67–98.

[35] Moatimid, G.M., Mohamed, M.A.A., and Elagamy, Kh., Prandtl-Eyring couple stressed flow within a porous region counting homogeneous and heterogeneous reactions across a stretched porous sheet, *Partial Differential Equations in Applied Mathematics*, 10, 2024, 100706.

[36] Zangooee, M.R., Hosseinzadeh, Kh., Ganji, D.D., Hydrothermal analysis of MHD nanofluid (TiO₂-GO) flow between two radiative stretchable rotating disks using AGM, *Case Studies in Thermal Engineering*, 14, 2019, 100460.

[37] Alwawi, F.A., Alkasasbeh, H.T., Rashad, A.M., Idris, R., MHD natural convection of Sodium Alginate Casson nanofluid over a solid sphere, *Results in Physics*, 16, 2020, 102818.

[38] Sayed, H.M., Aly, E.H., Tharwat, M.M., Mahros, A.M., Melting heat transfer and entropy analysis of ternary Casson nanofluids flow with second slip conditions: Application on rocket engine cooling, *Alexandria Engineering Journal*, 102, 2024, 10–25.

[39] Das, S.S., Ali, A., Jana, R.N., Makinde, O.D., EDL impact on mixed magneto-convection in a vertical channel using ternary hybrid nanofluid, *Chemical Engineering Journal Advances*, 12, 2022, 100412.

[40] Babu, M.J., Sandeep, N., 3D MHD slip flow of a nanofluid over a slendering stretching sheet with thermophoresis and Brownian motion effects, *Journal of Molecular Liquids*, 222, 2016, 1003–1009.

[41] Vajravelu, K., Dewasurendral, M., Prasad, K.V., Mixed convective boundary layer MHD flow along a vertical elastic sheet, *International Journal of Applied and Computational Mathematics*, 3, 2017, 2501–2518.

[42] Ramana Reddy, J.V., Sugunamma, V., Sandeep, N., Thermophoresis and Brownian motion effects on unsteady MHD nanofluid flow over a slandering stretching surface with slip effects, *Alexandria Engineering Journal*, 57, 2018, 2465–2473.

[43] Khan, M., Rasheed, A., Slip velocity and temperature jump effects on molybdenum disulfide MoS₂ and silicon oxide SiO₂ hybrid nanofluid near irregular 3D surface, *Alexandria Engineering Journal*, 60, 2021, 1689–1701.

[44] Salahuddin, T., Ali, Z., Awais, M., Khan, M., Altanji, M., A flow behavior of Sutterby nanofluid near the catalytic parabolic surface, *International Communications in Heat and Mass Transfer*, 131, 2022, 105821.

[45] Faisal, M., Mabood, F., Badruddin, I.A., Aiyaz, M., Butt, F.M., Entropic behavior with activation energy in the dynamics of hyperbolic-tangent mixed-convective nanomaterial due to a vertical slandering surface, *Multidiscipline Modeling in Materials and Structures*, 20(2), 2024, 341-362.

ORCID iD

Galal M. Moatimid https://orcid.org/0000-0001-6833-8903
Hamed M. Sayed https://orcid.org/0000-0002-2873-2110

Publisher's Note Shahid Chamran University of Ahvaz remains neutral with regard to jurisdictional claims in published maps and institutional affiliations.